CrossMark

ORIGINAL PAPER: CHARACTERIZATION METHODS OF SOL-GEL AND HYBRID MATERIALS

# Optimization of sol-gel synthesis parameters in the preparation of N-doped TiO$_2$ using surface response methodology

Shimelis Kebede Kassahun[1,2] · Zebene Kiflie[1] · Dong Woo Shin[3] · Sam Sik Park[3] ·
Won Young Jung[3] · Young Ryun Chung[2]

**Abstract** Response surface methodology, Box–Behnken experimental design, was applied to investigate and find optimum synthesis parameters for preparing visible-light active nitrogen-doped titanium dioxide by sol–gel method. Nitrogen to titanium molar ratios, calcination temperature, and calcination time have been selected as the study parameters. X-ray diffraction crystal phase compositions, Brunauer–Emmett–Teller-specific surface area, and visible-light decolorization of methylene blue have been examined as experimental responses. A total of 15 tests were conducted, and all the samples have demonstrated different photoactivity under visible light. Furthermore, the important synthesis parameters that affect the three selected responses were investigated using the analysis of variance. Calcination temperature was found to be the most significant parameter that has direct influence on the crystal phase compositions, the specific surface area, and photoactivity of the synthesized catalysts. The model adequacy test and regression analysis have shown that the results were well fitted with quadratic model equations. Model predictions were in good agreement with experimental data with 96.68, 96.88, and 96.96% variability. N/Ti molar ratio of 6, calcination temperature of 400 °C, and calcination time of 3 h was found to be the optimum condition. Sample prepared at the optimum condition was characterized and compared with the undoped sample and results show the successful preparation of the nitrogen-doped titanium dioxide.

## Graphical Abstract
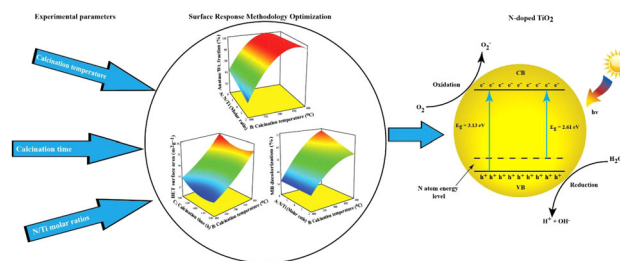
✉ Shimelis Kebede Kassahun
shimelis.kebede@aait.edu.et

1   School of Chemical and Bio Engineering, Addis Ababa Institute of Technology, Addis Ababa University, King George VI St, Addis Ababa, Ethiopia

2   Division of Applied Life Science (BK21 Plus Program), Plant Molecular Biology and Biotechnology Research Center, Gyeongsang National University, Jinju 52828, Korea

3   Nano Co., Ltd., 60 Magong-gongdan-ro, Cheongni, Sangju, Gyeongbuk 37257, Korea

## 1 Introduction

Response surface method (RSM) is one of the powerful statistical experimental design techniques that is applied to build models and investigate individual and interaction effects of the selected operating condition on the given response in a given experiment [1]. It is a very effective approach for optimization of complex processes in a more convenient way resulting in saving time, labor, and cost [2, 3]. Box–Behnken design (BBD) is one kind of RSM, which helps to design a second-order response model [4]. BBD

can provide a maximum amount of complex information with minimum experimental time [5]. Furthermore, in comparison with other statistical methods, such as full factorial design, it requires a few number of runs [6]. Most importantly, it avoids the analyses at their extreme combinations (such as at highest and lowest levels) for which unsatisfactory results might occur [7].

Titanium dioxide ($TiO_2$) is one of the most promising semiconductor materials that has attracted a lot of attention because of its successful application in different areas as a heterogeneous photocatalyst. Some of the main application areas include degradation of organic pollutants [8], inactivation of pathogenic microorganisms from water and air [9], and degradation of dyes [10, 11]. Relative inexpensiveness, high efficiency, environmentally friendliness, chemical and biological stabilities are its unique advantages [12, 13]. Most importantly, it can be used repeatedly with its catalytic capability for a long period of time [14]. However, its main drawback is that it is only activated by ultraviolet (UV) light, which accounts for 4–5% of the solar energy that reaches the earth's surface due to its wide band-gap energy (3.2 eV) [15].

So far, considerable efforts have been done in order to reduce its band-gap energy and utilize the visible-light which is the larger portion of the solar spectrum. One of the major approaches in this regard is doping, a modification of $TiO_2$ by influencing the electron structure with metal and non-metal ions [9, 16]. In comparison with the metal dopants, non-metals such as C, S, F, and N are effectively applied in the synthesis of visible-light active $TiO_2$ catalyst via band gap narrowing [17, 18]. After Asahi et al. [19], who first introduced successful doping of nitrogen and prepared a visible-light active $TiO_2$ in the wavelength range of less than 500 nm, nitrogen atom has been widely investigated [16, 18]. This is because nitrogen can be easily introduced into the titanium structure, as it has comparable atomic size and ionization energy [20]. There exist different physical and chemical synthesis routes that include implantation, sputtering, ball mill, solvothermal, and sol–gel methods for synthesis of nitrogen-doped titanium dioxide (N-doped $TiO_2$) [21, 22]. However, the sol–gel method seems to be by far advantageous over the other approaches. It is cheap, simple, and a low-temperature process. It requires no special equipment and offers relative ease to control the amount of dopant and crystal size [23–26]. Doping of non-metals with the sol–gel method depends on a number of synthesis parameters. These include amount and type of dopant, solvent type, solution pH, calcination temperature, and time. The proper incorporation of the dopant and properties of the final nanoparticles are highly influenced by these factors.

In most previous studies, it has been tried to investigate the effects of sol–gel synthesis parameters on the preparation of N-doped $TiO_2$ using the conventional "one-parameter-at-a-time approach". Although this approach is widely acceptable, it has a limitation in estimating the interaction effects between the factors and lacks a predictive capability [27].

In this paper, optimization of some of the significant sol–gel synthesis parameters by using BBD is reported. Nitrogen to titanium molar ratio (N/Ti), calcination temperature and calcination time to the response on anatase weight fraction ($W_A$), Brunauer–Emmett–Teller (BET)-specific surface area ($S_{BET}$), and photoactivity (methylene blue (MB) decolorization efficiency ($R$)) under visible-light sources on the prepared N-doped $TiO_2$ nanoparticles were investigated. Accordingly, the optimum BBD-based experimental values were found to be 100% ($W_A$), 87.12 $m^2 g^{-1}$ ($S_{BET}$), and 72.7% ($R$) for the conditions N/Ti molar ratio of 6, calcination temperature of 400 °C and calcination time of 3 h. Finally, doped and undoped $TiO_2$ samples were prepared at the optimum conditions and their chemical and physical properties were compared.

## 2 Experimental

### 2.1 Catalyst preparation

The BBD method was adopted to synthesize N-doped $TiO_2$ through sol–gel methods using ammonium hydroxide solution (28%) as a nitrogen source. Typically, 20 ml of a precursor solution titanium (IV) isopropoxide was slowly added to 100 ml of absolute ethanol, and the solution was adjusted to pH = 1 with nitric acid (60%). After 10 min of vigorous stirring on an ice bath, a different amount of ammonia solution was added to the prepared nano colloid solution to facilitate incorporation of nitrogen into $TiO_2$ crystal. The amounts of ammonia solution were adjusted to give N/Ti molar ratios of 2, 4, and 6 with vigorous stirring for 2 h. Subsequently, the mixtures were aged at room temperature for 24 h to allow further hydrolysis and then oven dried at 90 °C for 16 h to remove the solvent. The produced powder was then ground and calcined in a muffle furnace at a heating rate of 5 °C per minute under air. Three calcination temperatures (400, 500, and 600 °C), and three calcination times (3, 4, and 5 h) were used. Based on BBD, a total of 15 experimental runs were performed. After optimization the doped and undoped samples (with and without addition of ammonia as nitrogen source) were prepared using the optimum synthesis parameters. The N-doped $TiO_2$, and the undoped $TiO_2$ were designated as $xNTyz$, where $x$, $y$, and $z$, respectively, denote the N/Ti molar ratio, the calcination temperature, and time.

## 2.2 Photocatalytic activity

The photoactivity of N-doped $TiO_2$ nanoparticles was investigated using MB as a model chemical in batch photoreactor under visible-light irradiation. A 300-ml beaker was used as photoreactor for all experiments in which visible light was provided by Osram lamp (50 PARA30) with a wavelength of 400–700 nm. During this process, $1.0 \, g \, L^{-1}$ of the prepared powders were suspended in 100 ml of 10 ppm MB solution. The solution was continuously stirred with a magnetic stirrer to ensure homogenous mixing during 3-h irradiation period. Prior to proceeding to photoactivity test, the solution was stirred further for additional 30 min in dark environment to create adsorption-desorption equilibrium. After which, 10 ml of aliquots were taken from the reactor and filtered using 45-μm syringe filter. The MB concentration of supernatant was then analyzed with a portable spectrometer (DR 2700, Hach) at 664 nm wavelength absorbance. The MB decolorization efficiency ($R$) was calculated using the following equation:

$$R(\%) = \frac{C_o - C_f}{C_o} * (100), \tag{1}$$

where $C_o$ and $C_f$ are the concentrations of MB before and after visible-light irradiation.

## 2.3 Box–Behnken experimental design

The experiments were designed according to the Box–Behnken method with the selected three important sol–gel synthesis parameters as mentioned earlier. The required responses were optimized after studying the influences of these independent parameters and their interaction effects. The factors and levels are given in Table 1. The factors, i.e., N/Ti molar ratio, calcination temperature, and calcination time were designated as A, B, and C, respectively. According to BBD the total number of experiment can be calculated as:

$$N = k^2 + k + C_p, \tag{2}$$

where $k$ is a number of factors, and $C_p$ is a central replication point [5]. Table 2 shows the 15 experimental runs that are arranged according to BBD.

A second-order polynomial equation was used to find the relationship between the independent variables and the response. For the three chosen factors, the equation can be written as:

$$Y = \beta_0 + \beta_1 A + \beta_2 B + \beta_3 C + \beta_{12} AB + \beta_{13} AC + \beta_{23} BC \\ + \beta_{11} A^2 + \beta_{22} B^2 + \beta_{33} C^2 + \varepsilon, \tag{3}$$

where $\beta_0$ is a constant, A, B, and C are the independent variables, $\beta_i s$ are the coefficients for linear interaction effect, $\beta_{ii} s$ are the coefficients for cross-product interaction effect, $\beta_{ij} s$ are the coefficients for quadratic interaction effect, and $\varepsilon$ is the random error. The regression analysis and estimation of these coefficients were performed with a statistical software package Design-Expert® version 7.0.0 (Stat-Ease, Inc.). The adequacy of the model equations was evaluated using analysis of variance (ANOVA). Quality of fit of the model equations and their statistical significance were expressed using $F$-test, coefficient of determination ($R^2$), prediction coefficients of determination (Pred $R^2$), adjusted coefficients of determination (adj-$R^2$), and coefficients of variation (CV).

## 2.4 Catalyst characterization

The crystal phase compositions were obtained from the X-ray diffraction (XRD) measurement on PANalytical X'Pert PRO-MPD diffractometer with Cu-Kα radiation ($\lambda = 0.15406$), accelerating voltage (40 kV), and current (25 mA) at scan rate of 0.017 degree per minute in the range of $2\theta = 20^o$ to $85^o$. The average crystallite sizes of anatase and rutile phases were determined with the Scherrer equation .The weight fractions of the two phases were calculated using Spurr and Myers equation [28]. The specific surface area and pore volume and pore diameter were obtained from $N_2$ adsorption-desorption isotherm by using BET and Barett–Joyner–Halenda methods with Micromertics, Tristar II 3020. The structural properties were investigated by Raman spectrometer (Horiba/Jobin-Yvon, LabRAM HR800) with spectra resolution of $0.54 \, cm^{-1}$ in the range of $0$–$1000 \, cm^{-1}$ Raman shift. Analysis of functional groups was performed using Fourier Transformed Infrared (Varian 640-IR) FT–IR spectrometer, from $4000$–$400 \, cm^{-1}$ wavenumber. The binding energy and nitrogen content were

**Table 1** Experimental levels of selected variables for BBD

| Abbreviation | Levels | | | | |
| --- | --- | --- | --- | --- | --- |
| | Variables | Units | −1 (Low) | 0 (Medium) | +1 (High) |
| A | N/Ti | Molar ratio | 2 | 4 | 6 |
| B | Calcination temperature | $^o$C | 400 | 500 | 600 |
| C | Calcination time | h | 3 | 4 | 5 |

**Table 2** BBD with actual and predicted values of anatase weight fraction ($W_A$), BET-specific area ($S_{BET}$), and MB decolorization efficiency ($R$)

| Run | $A^a$ | $B^b$ | $C^c$ | $W_A$ (%) | | $S_{BET}$ (m² g⁻¹) | | $R$ (%) | |
|---|---|---|---|---|---|---|---|---|---|
| | | | | Actual value | Predicted value | Actual value | Predicted value | Actual value | Predicted value |
| 12 | 2 (−1) | 400 (−1) | 4 (0) | 100.00 | 100.31 | 80.18 | 80.60 | 59.01 | 60.12 |
| 5 | 6 (1) | 400 (−1) | 4 (0) | 100.00 | 99.62 | 77.07 | 78.17 | 74.77 | 73.52 |
| 15 | 2 (−1) | 600 (1) | 4 (0) | 91.67 | 92.05 | 30.81 | 29.71 | 34.92 | 36.18 |
| 13 | 6 (1) | 600 (1) | 4 (0) | 94.43 | 94.12 | 27.97 | 27.55 | 36.66 | 35.55 |
| 4 | 2 (−1) | 500 (0) | 3 (−1) | 100.00 | 99.73 | 63.32 | 61.88 | 56.71 | 55.61 |
| 10 | 6 (1) | 500 (0) | 3 (−1) | 100.00 | 100.42 | 62.51 | 60.39 | 60.55 | 61.81 |
| 14 | 2 (−1) | 500 (0) | 5 (1) | 100.00 | 99.57 | 51.15 | 53.27 | 54.74 | 53.48 |
| 11 | 6 (1) | 500 (0) | 5 (1) | 100.00 | 100.26 | 48.73 | 50.17 | 58.94 | 60.04 |
| 8 | 4 (0) | 400 (−1) | 3 (−1) | 100.00 | 99.96 | 87.58 | 88.60 | 68.32 | 68.31 |
| 7 | 4 (0) | 600 (1) | 3 (−1) | 93.52 | 93.40 | 37.99 | 40.53 | 36.10 | 35.95 |
| 1 | 4 (0) | 400 (−1) | 5(1) | 100.00 | 100.12 | 84.39 | 81.86 | 64.80 | 64.95 |
| 6 | 4 (0) | 600 (1) | 5 (1) | 92.88 | 92.92 | 29.46 | 28.44 | 35.40 | 35.41 |
| 3 | 4 (0) | 500 (0) | 4 (0) | 100.00 | 100.00 | 45.20 | 47.91 | 55.56 | 56.69 |
| 9 | 4 (0) | 500 (0) | 4 (0) | 100.00 | 100.00 | 47.24 | 47.91 | 57.37 | 56.69 |
| 2 | 4 (0) | 500 (0) | 4 (0) | 100.00 | 100.00 | 45.30 | 45.95 | 57.14 | 56.69 |

[a] N/Ti (molar ratio)

[b] Calcination temperature (°C)

[c] Calcination time (h)

estimated with X-ray photoelectron spectroscopy (XPS) (VG Microtech ESCA 2000) with Mg-Kα X-ray source ($hv = 1253.6$). The binding energy of carbon (C 1s: 284.8 eV) was used as an internal standard for the correction of charging shift, and the spectra was analyzed using CasaXPS software (version 2.3.17PR1.1). UV−Vis spectra of the samples was scanned using UV/Vis/NIR Spectrophotometer (Hitachi, U-4100) in the range of 200−800 nm. High-resolution transmission electron microscopy (HR-TEM) (TECHNAI G² F30 S-TWIN) operating at 300 kV was also used to investigate the average crystals size, morphology, and structure of the prepared nanoparticles. The surface morphologies and chemical composition of the syntheses samples were examined using field emission scanning electron microscope (FE-SEM) (JEOL JSM-7610F).

## 3 Results and discussion

### 3.1 Optimization of sol–gel synthesis parameters

Based on BBD and using the relationships in Table 1, a total of 15 experimental runs were performed including the central point that measures process stability and inherent variability. Figures 1 and 2 show XRD patterns and nitrogen adsorption-desorption isotherm of the as prepared N-doped $TiO_2$ samples according to BBD. The results from these two characterizations, $W_A$ and $S_{BET}$, were used as experimental response together with $R$ (Table 2).
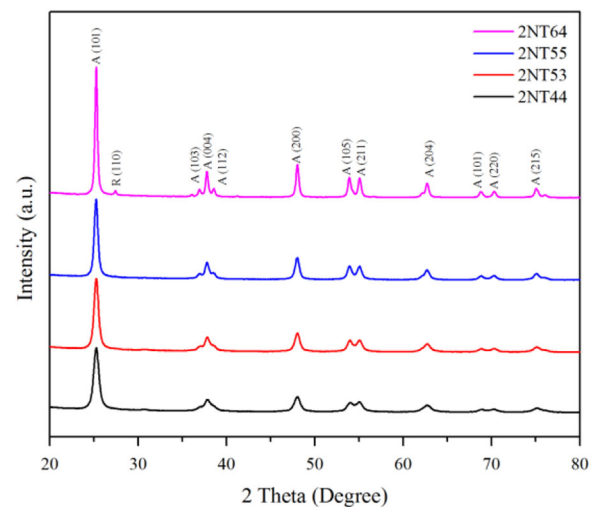


**Fig. 1** Selected XRD patterns of N-doped $TiO_2$ prepares at N/Ti molar ratio of 2

The analysis of the models indicates that they are highly significant with $F$-values of 77.57 for ($W_A$), 94.95 for ($S_{BET}$), and 92.23 for ($R$) with their corresponding $P$-value $< 0.0001$. The ANOVA for the three selected responses is shown in Supplementary Information Tables S1, S2, and S3. The mutual interaction between the test variables can be revealed using $P$-values [29].

The model adequacy was further investigated using $R^2$ for the three responses ($W_A$, $S_{BET}$, and $R$), which were found to be 0.9929, 0.9942, and 0.994, respectively. These
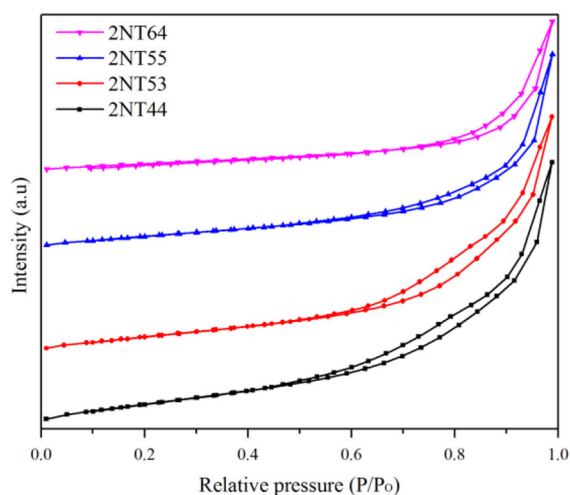
**Fig. 2** Selected nitrogen adsorption-desorption isotherms of N-doped TiO$_2$ prepares at N/Ti molar ratio of 2

imply that the models are adequate enough to predict the response in the experimental range with 99.29, 99.42, and 99.40% variability. The experimentally found and the predicted values were in a good agreement as depicted in Table 2. The Pred $R^2$ show that the model equations for $W_A$, $S_{BET}$, and $R$ give good predictions with 88.62, 91.30, and 91.63% variability, respectively. In addition, the adj-$R^2$ of $W_A$ (98.01%), $S_{BET}$ (98.37%), and $R$ (98.32%) were in a reasonable agreement with Pred $R^2$ values. The degree of precision and reliability can be explained by the low values of CV, which were 0.46 for $W_A$, 4.73 for $S_{BET}$, and 3.01 for $R$. Furthermore, adequacy precision for each response ($W_A$, $S_{BET}$, and $R$) was found to be 22.76, 28.961, and 28.701. All the above values can be changed when only the significant terms are considered (see Supplementary Information Table S4). The values of "Prob > $F$" less than 0.05 indicate model terms are significant.

Based on regression analysis the quadratic model equations for the three responses, $W_A$, $S_{BET}$, and $R$, in terms of actual values can be written by considering the significant terms as follows:

$$W_A(\%) = 37.46 - 1.55250A + 0.2955B + 0.00345AB \\ - 0.00034375B^2 \tag{4}$$

$$S_{BET}(m^2 g^{-1}) = 477.34258 - 5.2024A - 70.00342C \\ + 0.5758A^2 + 0.000574B^2 + 8016183C^2 \tag{5}$$

$$R(\%) = -53.85143 + 10.35875A + 0.51929B \\ - 0.975C - 0.017525AB - 0.00060394B^2. \tag{6}$$

### 3.2 Crystal phase composition

Figure 1 shows selected XRD patterns for the N-doped TiO$_2$ samples prepared under different calcination temperatures, calcination times, and similar nitrogen to titanium molar ratios. The crystal phases were well much with (JCPDS) Card No 21-1272 and 21-1276 for anatase and rutile, respectively. It can be observed that no peak associated with nitrogen was revealed in all of the XRD patterns. This might due to the dopant is uniformly distributed either in the TiO$_2$ crystal structure occupying interstitial or substitutional sites [30–32]. However, Fig. 1 indicates that the two crystal phases (anatase and rutile) appear at different sol–gel operational parameters with the anatase phase being dominant at calcination temperatures below 600 °C. Similarly, as can be observed from Fig. 3a, at high calcination temperature (600 °C), the phase transformation process is seen to be slightly retarded with increasing nitrogen concentration from 2 to 6 N/Ti molar ratio. This result suggests that the thermal stability of the catalyst can be improved by the addition of nitrogen [33]. The effect of the presence of nitrogen on phase composition of TiO$_2$ can be further evidenced from Fig. S1 (Supplementary Information), where the XRD pattern of the undoped TiO$_2$ catalyst prepared at the optimum condition (400 °C, 3 h) is presented. As can be observed, the presence of rutile is quite evident and its amount is estimated to be about 12.87%. However, comparison with Fig. 1 shows that rutile phase was not detected in the N-doped TiO$_2$ samples prepared below 600 °C. The presence of rutile at 400 °C in the undoped sample can be related to the lower pH of the solution as reported by Matthews [34].

In addition, Fig. 1 depicts that as the calcination temperature increased from 400 to 600 °C, the anatase peak became sharper and more intense. The average crystal size of all samples increased with the calcination temperature, which is due to the formation of bigger crystallite aggregation of the catalyst at higher temperature [35]. As compared with the effect calcination temperature, the effect of nitrogen on crystal structure and particle size was minimum in all samples. The effect of calcination time was also found to be insignificant in this study (Fig. 3b). The crystallite size of each sample was calculated according to Scherrer formula and presented in Table S5 (Supplementary Information).

### 3.3 Specific surface area

Selected N$_2$ adsorption-desorption isotherms for different N-doped TiO$_2$ are given in Fig. 2. The specific surface areas of the synthesized samples are found to be more dependent on calcination temperature than on calcination time and N/Ti molar ratio as shown in Table 2. Generally, all N-doped
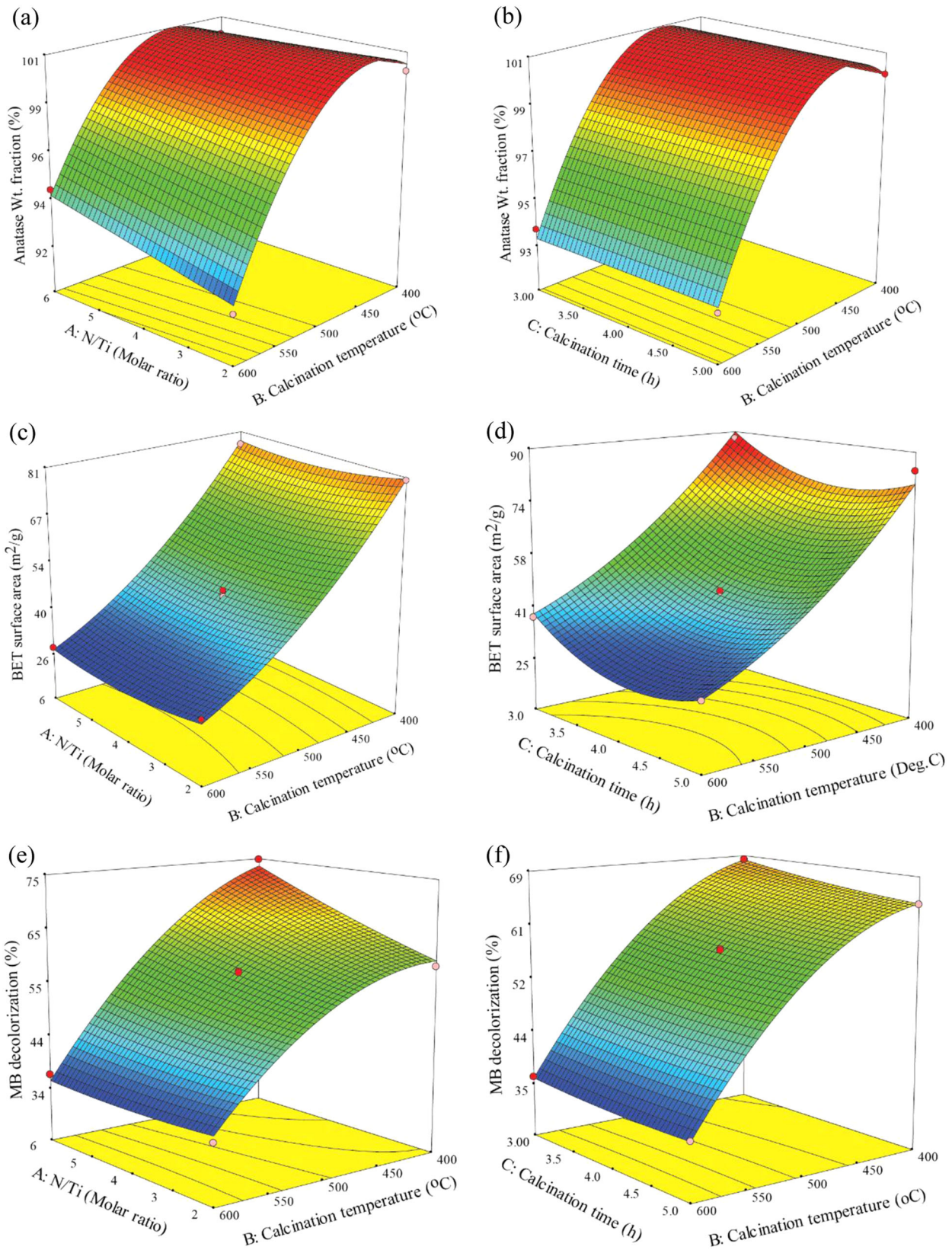
**Fig. 3** Three-dimensional response plots showing interaction effects of N/Ti molar ratio, calcination temperature, and time on anatase wt. fraction (**a**) and (**b**), on BET surface area (**c**) and (**d**), on MB decolorization (**e**) and (**f**)

TiO$_2$ samples prepared at lower and higher calcination temperature demonstrated smaller and larger mesopore structures, respectively. A plausible explanation can be at higher calcination temperature and extended calcination time, there is an expansion of mesopores and consequently the formation of bigger pores [36]. The specific surface areas also indicated a decreasing trend with increase in calcination temperature and time (Fig. 3c, d). Decreased specific surface area is due to catalyst aggregation at the higher temperature [37]. In addition, the specific surface area and crystal size of the undoped sample were found to be larger than those of the doped TiO$_2$, although the total pore size of the N-doped TiO$_2$ sample was higher as compared with that of the undoped TiO$_2$ sample (Supplementary Information Fig. S2). It can be attributed to the three-dimensional network microstructure, which was formed between the N-doped TiO$_2$ catalyst particles [18, 30, 38, 39].

### 3.4 Photoactivity test

The photocatalytic performance of all synthesized N-doped TiO$_2$ samples was examined by decolorization of MB in the liquid solution with visible light ($\lambda > 400$ nm). The samples at higher calcination temperature exhibited the lowest percentage of decolorization of MB as shown in Fig. 3e and f. Significant specific surface area reduction and larger particle size at elevated calcination temperature and time might have led to lowest decolorization. It was also observed that the decolorization efficiency increased remarkably when the amount of N dopants increased from 2 to 6 N/Ti molar ratio and at lower calcination temperature (Fig. 3e). A possible explanation for this condition is that a higher concentration of N dopant facilitated proper incorporation of nitrogen into the TiO$_2$ structure and consequently increased the visible-light activity of TiO$_2$. All samples that were prepared at lower calcination temperatures and higher N concentrations have larger surface area, which provided better adsorption of reactive molecules as the most active sites are those on the surface [40]. Furthermore, these also helped to improve the light harvesting on the larger surface area but with fewer degrees [41]. Though, the nitrogen dopant amount and the higher specific surface area were the main factors for high photoactivity in the present study, particle size and crystallinity also played important role. Lower photoactivity can be caused by the charge recombination, which is associated with low crystallinity and larger particle size [42, 43]. As a matter of fact, the highest photocatalytic activity shown by the N-doped TiO$_2$ sample prepared at N/Ti molar ratio of 6 and calcined at 400 $^\circ$C for 4 h can be related to its high specific surface area, nitrogen content, and improved anatase crystallinity.

**Table 3** Model validation results of doped and undoped TiO$_2$ prepared under optimized condition

| Sample | Crystal phase composition (%) | | Crystal size (nm) | | $S_{BET}$ (m$^2$ g$^{-1}$) | $R$ (%) |
|---|---|---|---|---|---|---|
| | ($W_A$) | ($W_R$) | Anatase | Rutile | | |
| 6NT43 | 100 | – | 10.14 | – | 87.12 | 72.7 ± 1.54 |
| 0NT43 | 87.13 | 12.87 | 8.27 | 19.96 | 92.84 | 11.8 ± 0.56 |

*Note*: $W_A$: anatase weight fraction, $W_R$: rutile weight fraction, $S_{BET}$: BET surface area, $R$: MB decolorization efficiency

### 3.5 Model optimization and verification

Based on Derringer's desirability function approach for multiple response processes, the desired set of sol–gel synthesis parameters were determined through optimization of the responses from the three quadratic models (Eqs 4, 5, and 6). Accordingly, N/Ti molar ratio of 6, calcination temperature of 400 °C, and calcination time of 3 h (6NT43) were selected with 0.987 desirability to predict anatase weight fraction of 100%, BET surface area of 90.99 m$^2$ g$^{-1}$, and MB decolorization efficiency of 74%. The predicted values were also validated on sample prepared under the optimum condition (Table 3). The results show that with the given Pred $R^2$ for each response, the model equations can be potentially used to predict sol–gel synthesis parameters in the same preparation routes.

### 3.6 Characterization of doped and undoped samples prepared under optimum conditions

#### 3.6.1 XPS analysis

The elemental analysis and chemical binding energy of the prepared sample were determined using XPS. Figure 4 shows the high-resolution spectra of N-doped TiO$_2$ sample, which was prepared under the optimum condition. From the deconvolution of the N 1s peaks of high-resolution spectra, the atomic concentration of N was found to be around 2.79% for N-doped TiO$_2$ (6NT43). The three peaks were detected at 397.06, 400.03, and 404.13 eV binding energies. The exact positions of N atoms are still unclear and under debates. Many previously done studies assigned the position at the various locations from 395–404 eV binding energy based on their preparation routes and nitrogen source. However, in some of the well-known articles, the binding energy of N at 396 eV was surely assigned for atomic β-N [19, 44, 45]. This binding energy can be further extended to around 397 eV [46, 47]. At this site, a substitutional replacement of oxygen by nitrogen takes place within TiO$_2$ crystal lattice in the form of Ti−N−Ti entity and may act, for visible light, as active site [48]. On the other
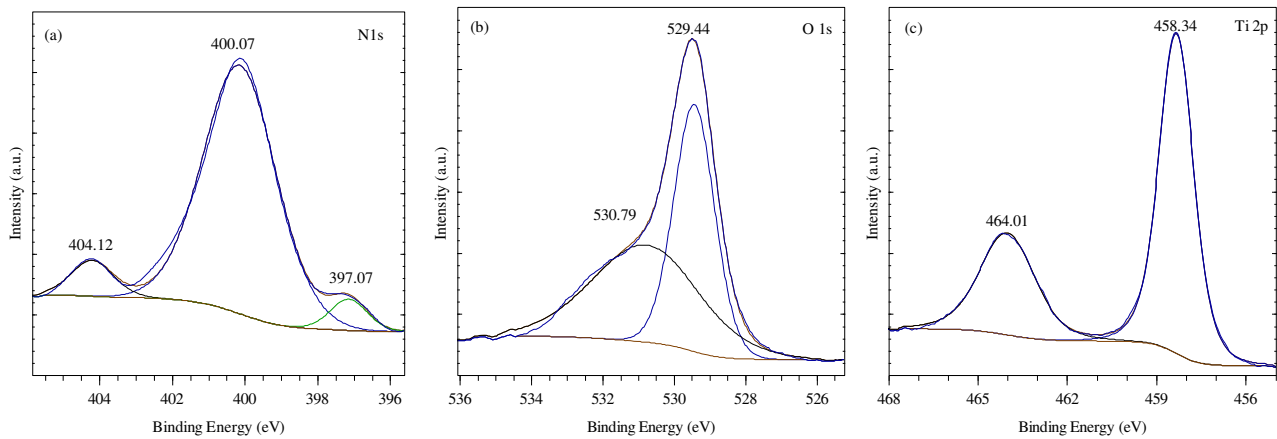
Fig. 4 XPS spectra of N-doped TiO$_2$ prepared under optimum condition

hand, for interstitial N-doped TiO$_2$ such as Ti–N–O and/or Ti–O–N oxynitride, there is no common agreement. Generally, the peak approximate to 400 eV is assigned for interstitial N-doping [44, 49]. The binding energy around 397 eV has also as been assigned for interstitial N-doping by some authors [45, 50]. In the present study, the peaks at 397.07 and 400.07 eV are assigned for substitutional N-doping. Whereas, the other peak at 404.12 was assigned to nitrite (NO$_2^-$). The peak for O 1s core level of the N-doped TiO$_2$ is located at 529.44 eV (Fig. 4b) and the peak for the undoped TiO$_2$ appears at 529.13 eV (Supplementary Information Fig. S3a). Comparison of the two figures shows that the peak for the undoped sample has decreased by 0.31 eV. Furthermore, Ti 2p$_{3/2}$ and 2p$_{1/2}$ core level peaks appear at 458.34 and 464.01 eV for the doped and at 457.99 and 463.66 eV for the undoped TiO$_2$ samples (Fig. 4c and Supplementary Information Fig. S3b). These results indicate that the binding energy of undoped TiO$_2$ shifts toward lower binding energy by 0.35 eV from doped TiO$_2$. The binding energy shifts observed in both cases imply that the TiO$_2$ crystal lattice was modified by the addition of nitrogen.

### 3.6.2 UV/Vis analysis

UV/Vis/NIR spectrophotometer was used to evaluate optical properties of both undoped and doped TiO$_2$ samples. For comparison, the maximum optical absorption edge ($\lambda_g$) of N-doped TiO$_2$, which was prepared with optimized parameters (6NT43) and undoped sample (0NT43), is shown in Table 4. The band-gap energy ($E_g$) of each sample was calculated using the formula:

$$E_g(eV) = \frac{1240}{\lambda_g}, \tag{7}$$

Table 4 Maximum adsorption edge and corresponding band-gap energy of N-doped and undoped TiO$_2$

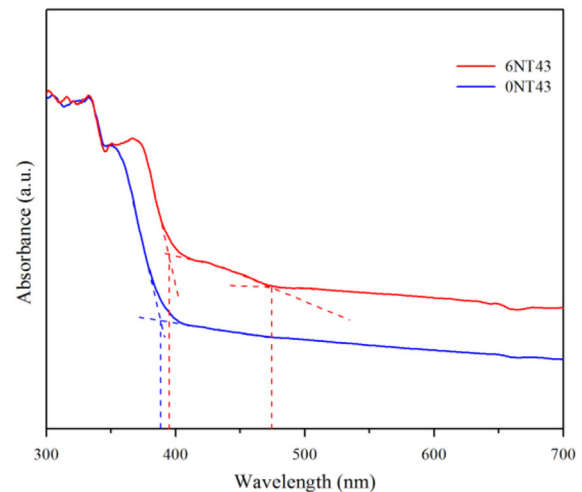| Sample | $\lambda_{g,1}$ (nm) | $E_{g,1}$ (eV) | $\lambda_{g,2}$ (nm) | $E_{g,2}$ (eV) |
|--------|------|------|------|------|
| 6NT43 | 395 | 3.13 | 475 | 2.61 |
| 0NT43 | 388 | 3.19 | – | – |



Fig. 5 UV–Vis spectra of undoped and doped TiO$_2$ prepared under optimum condition

Many researchers pointed out that the preparation of N-doped TiO$_2$ shows spectra shift toward the visible-light region [18, 41]. Asahi et al. claim that its visible-light photoactivity can be related to narrowed band gap by mixing of nitrogen 2p and oxygen 2p state in the valence band caused by substitutional doping [19]. In contrast, Burda and his coworker have stated that the extra electronic states just above the valence band edge were the main reasons behind this phenomenon [47]. On the other
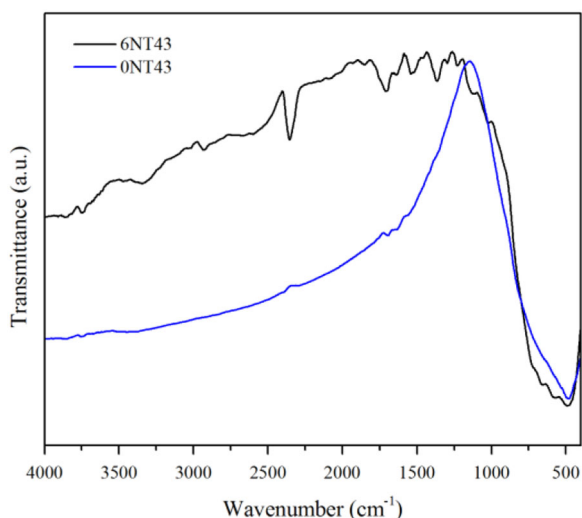
Fig. 6 FT–IR spectra of undoped and doped $TiO_2$ prepared under optimum condition
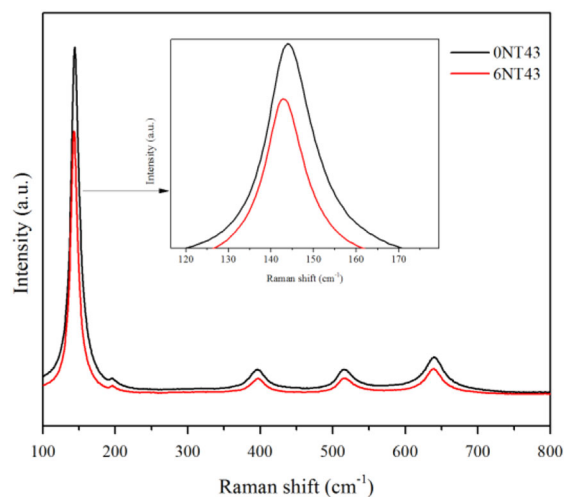


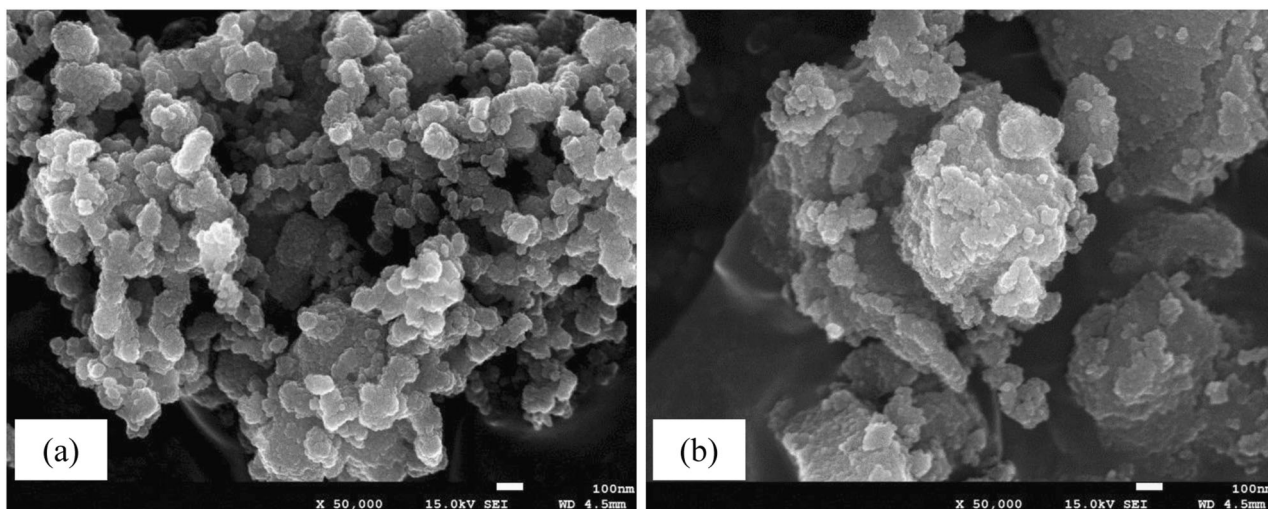Fig. 7 Raman spectra of undoped and doped $TiO_2$ prepared under optimum condition



Fig. 8 FE-SEM images of doped $TiO_2$ (**a**), and undoped $TiO_2$ (**b**), prepared under optimum condition

hand, other reports state that it is either the isolated N impurity energy level (N 2p localized states) forms above the O 2p valence band (0.14 eV) in the case of substitutional doping or the Л* character generated by NO bond slightly above the valence band (0.73) in the case of interstitial doping that caused a visible-light active N-doped $TiO_2$ photocatalyst [51–54]. Furthermore, the formation of oxygen vacancies between the valence and conduction bands during thermal treatment enhance the photocatalysis in the visible range above 500 nm [35, 52, 55–57]. In this study, in contrast with undoped $TiO_2$, the N-doped sample (6NT43) provides two absorption edges; one at 395 nm due to intrinsic band-gap absorption typical for anatase in UV region (<400 nm) and other additional

edge at 475 nm, which can be attributed to extrinsic electronic levels due to interstitial nitrogen doping (Fig. 5). This result exhibited the successful doping of nitrogen in $TiO_2$ lattice.

### 3.6.3 FT–IR analysis

The FT–IR spectra of N-doped and undoped $TiO_2$ samples is presented in Fig. 6. For N-doped $TiO_2$ FT–IR characterization, the absorption peaks that are located at around 3100–3500 and 1630–1645 $cm^{-1}$ assigned to stretching and bending vibrations of O–H bond in hydroxyls group and adsorbed water on the surface of $TiO_2$ [58, 59]. In the present study, these peak intensities were presented at 3344
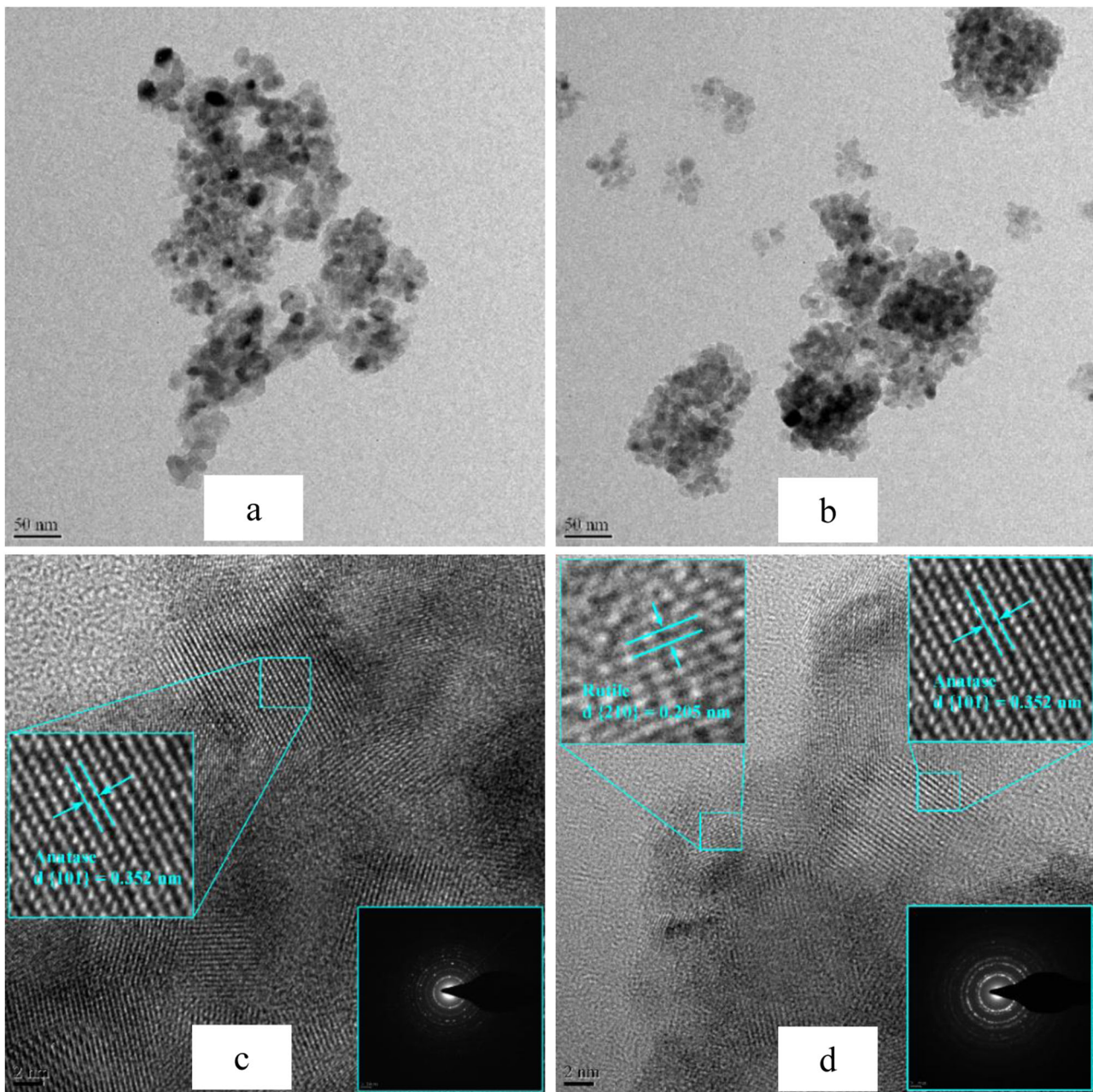
**Fig. 9** HR-TEM images and corresponding interplanar space of doped TiO$_2$ (**a**) and (**c**), undoped TiO$_2$ (**b**) and (**d**)

and 1637 cm$^{-1}$ and were stronger than those of the undoped TiO$_2$. The adsorbed OH groups are helpful to improve photocatalytic activity of N-doped TiO$_2$ by serving as an oxidizer for degradation of organic pollutant and giving better charge transfer by interacting the photogenerated holes [21, 59]. Furthermore, on N-doped TiO$_2$ sample, multi-peaks were shown on the spectra range from 1000 to 1600 cm$^{-1}$ which could be ascribed to different nitrogen species [60]. Especially the strong peak at around 1110–1020 cm$^{-1}$ may be due to the formation of hyponitrite species [51, 60]. The appearance of these peaks gives

additional evidence and further confirmation for the successful doping of N into the TiO$_2$ crystal. The other strong peaks in the region 480–700 cm$^{-1}$ corresponded to Ti-O stretching vibration [59, 61, 62].

### 3.6.4 Raman analysis

Raman spectra of N-doped and undoped TiO$_2$ samples are shown in Fig. 7. Both samples show typical anatase crystalline phase with major bands at 144, 196, 397, 519, and 639 cm$^{-1}$. Moreover, the doped sample did not indicate the

presence of nitrogen, which may be because nitrogen is incorporated in the form of interstitial doping. In contrast to the XRD analysis, Raman analysis did not show the presence of rutile phase. This is because at the low rutile mass fraction, Raman spectroscopy can be used only to detect the presence of $TiO_2$ but not for phase identification [33]. Moreover, the Raman shift can help to identify the particle size difference between doped and undoped $TiO_2$. Noticeably, the peak at $144\,cm^{-1}$ slightly shifts toward the lower band for doped $TiO_2$, indicating slightly higher crystal size. This observation is in agreement with the results of XRD analysis, which showed that the addition of nitrogen can enhance the growth of crystals.

### 3.6.5 FE-SEM analysis

FE-SEM images of N-doped and undoped $TiO_2$ are shown in Fig. 8. As it can be clearly observed from the figure, the nanoparticles in both samples appeared to be agglomerated. However, the N-doped $TiO_2$ sample exhibited well-dispersed particles and a large number of pores. This may be a result of decomposition of ammonia into different gases during heating process. This result is consistent with the BET analysis, which revealed a mesoporous structure. Generally, with this structure, it is possible to achieve enhanced photocatalytic activity as it promotes diffusion and access to reactive sites on the surface of the catalyst [63]. Furthermore, the particles in N-doped $TiO_2$ sample have also shown irregular spherical shape.

### 3.6.6 HR-TEM analysis

The morphology and crystal size of N-doped and undoped catalysts are shown in Fig. 9. The $TiO_2$ particles are seen to be more dispersed in the N-doped sample, while more agglomerated in the undoped sample. The average crystallite size was estimated from HR-TEM analysis, and was found to be in the range of 10–21 and 8–16 nm for the N-doped and undoped $TiO_2$ samples, respectively. The fact that larger crystal size was observed for N-doped $TiO_2$ in both HR-TEM and XRD analysis suggests that the addition of nitrogen can improve the crystal size growth of $TiO_2$ [33, 64, 65]. Furthermore, the interplanar distances $d = 0.205$ nm for rutile and $d = 0.352$ nm for anatase at (210) and (101) planes indicate good crystallinity. In the case of N-doped sample, there was no significant change in lattice space due to the addition of nitrogen.

## 4 Conclusions

In this study, the sol–gel synthesis parameters for the preparation of N-doped $TiO_2$ were investigated and optimized using the BBD RSM. The study has shown that the experimental method can be used as an excellent tool to identify the interaction effect of the individual sol–gel synthesis parameters. It was also found possible to gather sufficient information about the synthesis method with a limited number of trials. Under optimized process condition, 100% anatase crystalline phase, BET surface area of $90.99\,m^2\,g^{-1}$, and MB decolorization efficiency of 74% were predicted. It is worth to note that all characterization techniques used in the present study have confirmed the successful preparation of visible-light active N-doped $TiO_2$ with higher specific surface area, larger pore size, smaller crystal size, good crystallinity, and anatase crystal phase.

**Compliance with ethical standards**

**Conflict of interest** The authors declare that they have no conflict of interest.

## References

1. Dong CH, Xie XQ, Wang XL, Zhan Y, Yao YJ (2009) Application of Box–Behnken design in optimisation for polysaccharides extraction from cultured mycelium of Cordyceps sinensis. Food Bioprod Process 87:139–144

2. Lee K, Hamid S (2015) Simple response surface methodology: investigation on advance photocatalytic oxidation of 4-chlorophenoxyacetic acid using UV-active ZnO photocatalyst. Materials 8:339–354

3. Safari M, Rostami MH, Alizadeh M, Alizadehbirjandi A, Nakhli SAA, Aminzadeh R (2014) Response surface analysis of photocatalytic degradation of methyl tert-butyl ether by core/shell $Fe_3O_4$/ZnO nanoparticles. J Environ Heal Sci Eng 12:1–10

4. Tekindal MA, Bayrak H, Ozkaya B, Genc Y (2012) Box–Behnken experimental design in factorial experiments: the importance of bread for nutrition and health. Turkish J F Crop 17:115–123

5. Aslan N, Cebeci Y (2007) Application of Box–Behnken design and response surface methodology for modeling of some. Turkish coals Fuel 86:90–97

6. Lotfizadehdehkordi B, Ghadimi A, Metselaar HSC (2013) Box–Behnken experimental design for investigation of stability and thermal conductivity of $TiO_2$ nanofluids. J Nanoparticle Res 15:1369

7. Ferreira SLC, Bruns RE, Ferreira HS, Matos GD, David JM, Brandão GC, Da Silva EGP, Portugal LA, Dos Reis PS, Souza AS, Dos Santos WNL (2007) Box–Behnken design: an alternative for the optimization of analytical methods. Anal Chim Acta 597:179–186

8. Huang X, Tang Y, Hu C, Yu H, Chen C (2005) Preparation and characterization of visible-light-active nitrogen-doped $TiO_2$ photocatalyst. J Environ Sci 17:562–565

9. Ferrari-Lima AM, Marques RG, Gimenes ML, Fernandes-Machado NRC (2014) Synthesis, characterisation and photocatalytic activity of N-doped $TiO_2$-$Nb_2O_5$ mixed oxides. Catal Today 254:119–128

10. Natarajan K, Natarajan TS, Bajaj HC, Tayade RJ (2011) Photocatalytic reactor based on UV-LED/$TiO_2$ coated quartz tube for degradation of dyes. Chem Eng J 178:40–49

11. Khataee AR, Zarei M, Moradkhannejhad L, Nourie S, Vahid B (2013) Nitrogen doping of commercial $TiO_2$ nanoparticles for enhanced photocatalytic degradation of dye under visible light: central composite design approach. Adv Chem Lett 1:24–31

12. Di Paola A, Bellardita M, Palmisano L (2013) Brookite, the least known $TiO_2$ photocatalyst. Catalysts 18:36–73

13. Gupta SM, Tripathi M (2011) A review of $TiO_2$ nanoparticles. Chinese Sci Bull 56:1639–1657

14. Zhang Z, Gamage J (2010) Applications of photocatalytic disinfection. Int J Photoenergy 2010:1–11

15. Luo N, Jiang Z, Shi H, Cao F, Xiao T, Edwards PP (2009) Photocatalytic conversion of oxygenated hydrocarbons to hydrogen over heteroatom-doped $TiO_2$ catalysts. Int J Hydrogen Energy 34:125–129

16. Zhu M, Zhai C, Qiu L, Lu C, Paton AS, Du Y, Goh M (2015) New method to synthesize S-doped $TiO_2$ with stable and highly efficient photocatalytic performance under indoor sunlight irradiation. ACS Sustainable Chem Eng 3:3123–3129

17. Caratto V, Setti L, Campodonico S, Carnasciali MM, Botter R, Ferretti M (2012) Synthesis and characterization of nitrogen-doped $TiO_2$ nanoparticles prepared by sol–gel method. J Sol-Gel Sci Technol 63:16–22

18. Lee HU, Lee SC, Choi S, Son B, Lee SM, Kim HJ, Lee J (2013) Efficient visible-light induced photocatalysis on nanoporous nitrogen-doped titanium dioxide catalysts. Chem Eng J 228:756–764

19. Asahi R (2001) Visible-light photocatalysis in nitrogen-doped titanium oxides. Science 293:269–271

20. Jo W, Shin S, Chun H (2014) Application of glass fiber-based N-doped titania under visible-light exposure for photocatalytic degradation of aromatic pollutants. Int J Photoenergy 2014:1–9

21. Wang T, Yan X, Zhao S, Lin B, Xue C, Yang G, Ding S, Yang B, Ma C, Yang G, Yang G (2014) A facile one-step synthesis of three-dimensionally ordered macroporous N-doped $TiO_2$ with ethanediamine as the nitrogen source. J Mater Chem A 2:15611–15619

22. Le TS, Ngo QB, Nguyen VD, Nguyen HC, Dao TH, Tran XT, Kabachkov EN, Balikhin IL (2014) Photocatalytic equipment with nitrogen-doped titanium dioxide for air cleaning and disinfecting. Adv Nat Sci Nanosci Nanotechnol 5:1–6

23. Nishikiori H, Hayashibe M, Fujii T (2013) Visible light-photocatalytic activity of sulfate-doped titanium dioxide prepared by the sol−gel method. Catalysts 3:363–377

24. Perumal S, Sambandam CG, Monikanda K, Ananthakumar S (2014) Synthesis and charecterization studies of nano $TiO_2$ prepared via sol-gel method. IJRET Int J Res Eng Technol 3:651–657

25. Macwan DP, Dave PN, Chaturvedi S (2011) A review on nano-$TiO_2$ sol–gel type syntheses and its applications. J Mater Sci 46:3669–3686

26. Zhang W, Zou L, Lewis R, Dionysio D (2014) A review of visible-light sensitive $TiO_2$ synthesis via sol-gel N-doping for the degradation of dissolved organic compounds in wastewater treatment. J Mater Sci Chem Eng 2:28–40

27. Chong MN, Jin B, Chow CWK, Saint C (2010) Recent developments in photocatalytic water treatment technology: a review. Water Res 44:2997–3027

28. Hanaor DAH, Chironi I, Karatchevtseva I, Triani G, Sorrell CC (2012) Single and mixed phase $TiO_2$ powders prepared by excess hydrolysis of titanium alkoxide. Adv Appl Ceram 111:149–158

29. Vimalashanmugam TV K (2012) Response surface methodology optimization of process parameters for xylanase production by aspergillus fumigatus in SSF using central composite design. Int J Eng Res Appl 2:277–287

30. Hui-Lei W, Xiao-Heng L (2014) Synthesis of N-doped mesoporous titania with high visible-light photocatalytic activity. J Inorg Mater 29:997–1002

31. Li X, Liu P, Mao Y, Xing M, Zhang J (2015) Preparation of homogeneous nitrogen-doped mesoporous $TiO_2$ spheres with enhanced visible-light photocatalysis. Appl Catal B Environ 164:352–359

32. Lin YT, Weng CH, Hsu HJ, Lin YH, Shiesh CC (2013) The synergistic effect of nitrogen dopant and calcination temperature on the visible-light-induced photoactivity of N-doped $TiO_2$. Int J Photoenergy 2013:1–13

33. Samsudin EM, Abd Hamid SB, Juan JC, Basirun WJ, Kandjani AE, Bhargava SK (2015) Controlled nitrogen insertion in titanium dioxide for optimal photocatalytic degradation of atrazine. RSC Adv 5:44041–44052

34. Matthews A (1976) The crystallization of anatase and rutile titanium dioxide under hydrothermal conditions. Am Mineral 61:419–424

35. Lin Y-H, Weng C-H, Srivastav AL, Lin Y-T, Tzeng J-H (2015) Facile synthesis and characterization of N-doped $TiO_2$ photocatalyst and its visible-light activity for photo-oxidation of ethylene. J Nanomater 2015:1–10

36. Zhu J, Wang T, Xu X, Xiao P, Li J (2013) Pt nanoparticles supported on SBA-15: synthesis, characterization and applications in heterogeneous catalysis. Appl Catal B Environ 130–131:197–217

37. Yu H, Zheng X, Yin Z, Tag F, Fang B, Hou K (2007) Preparation of nitrogen-doped $TiO_2$ nanoparticle catalyst and its catalytic activity under visible light. Chinese J Chem Eng 15:802–805

38. Qin HL, Gu GB, Liu S (2008) Preparation of nitrogen-doped titania using sol-gel technique and its photocatalytic activity. Mater Chem Phys 112:346–352

39. Horikawa T, Katoh M, Tomida T (2008) Preparation and characterization of nitrogen-doped mesoporous titania with high specific surface area. Micropor Mesopor Mat 110:397–404

40. Wei X, Zhu G, Fang J, Chen J (2013) Synthesis, characterization, and photocatalysis of well-dispersible phase-pure anatase $TiO_2$ nanoparticles. Int J Photoenergy 2013:1–6

41. Liu K-I, Su C-Y, Perng T-P (2015) Highly porous N-doped $TiO_2$ hollow fibers with internal three-dimensional interconnected nanotubes for photocatalytic hydrogen production. RSC Adv 5:88367–88374

42. Li G, Chen L, Graham ME, Gray KA (2007) A comparison of mixed phase titania photocatalysts prepared by physical and chemical methods: the importance of the solid-solid interface. J Mol Catal A Chem 275:30–35

43. Rengifo-Herrera JA, Mielczarski E, Mielczarski J, Castillo NC, Kiwi J, Pulgarin C (2008) *Escherichia coli* inactivation by N, S co-doped commercial $TiO_2$ powders under UV and visible light. Appl Catal B Environ 84:448–456

44. Sato S, Nakamura R, Abe S (2005) Visible-light sensitization of $TiO_2$ photocatalysts by wet-method N doping. Appl Catal A Gen 284:131–137

45. Saha NC, Tompkins HG (1992) Titanium nitride oxidation chemistry: an X-ray photoelectron spectroscopy study. J Appl Phys 72:3072–3079

46. Buzby S, Barakat MA, Lin H, Ni C, Rykov SA, Chen JG, Ismat Shah S (2006) Visible light photocatalysis with nitrogen-doped titanium dioxide nanoparticles prepared by plasma assisted

chemical vapor deposition. J Vac Sci Technol B Microelectron Nanom Struct 24:1210–1214

47. Chen X, Chen X, Burda C, Burda C (2008) The electronic origin of the visible-light absorption properties of C-, N- and S-doped $TiO_2$ nanomaterials. J Am Chem Soc 130:5018–5019

48. Mollavali M, Falamaki C, Rohani S (2015) Preparation of multiple-doped $TiO_2$ nanotube arrays with nitrogen, carbon and nickel with enhanced visible light photoelectrochemical activity via single-step anodization. Int J Hydrogen Energy 40:12239–12252

49. Wang J, Tafen DN, Lewis JP, Hong Z, Manivannan A, Zhi M, Li M, Mu N (2009) Origin of photocatalytic activity of nitrogen-doped $TiO_2$ nanobelts. J Am Chem Soc 131:12290–12297

50. Chan MH, Lu FH (2008) Preparation of titanium oxynitride thin films by reactive sputtering using air/Ar mixtures. Surf Coatings Technol 203:614–618

51. Peng F, Cai L, Yu H, Wang H, Yang J (2008) Synthesis and characterization of substitutional and interstitial nitrogen-doped titanium dioxides with visible light photocatalytic activity. J Solid State Chem 181:130–136

52. Lin Z, Orlov A, Lambert RM, Payne MC (2005) New insights into the origin of visible light photocatalytic activity of nitrogen-doped and oxygen-deficient anatase $TiO_2$. J Phys Chem B 109:20948–20952

53. Di Valentin C, Pacchioni G, Selloni A, Livraghi S, Giamello E (2005) Characterization of paramagnetic species in N-doped $TiO_2$ powders by EPR spectroscopy and DFT calculations. J Phys Chem B 109:11414–11419

54. Irie H, Watanabe Y, Hashimoto K (2003) Nitrogen-concentration dependence on photocatalytic activity of $TiO_{2-x}N_x$ powders. J Phys Chem B 10:5483–5486

55. Di Valentin C, Pacchioni G, Selloni A (2004) Origin of the different photoactivity of N-doped anatase and rutile $TiO_2$. Phys Rev B 70:85116

56. Nakamura I, Negishi N, Kutsuna S, Ihara T, Sugihara S, Takeuchi K (2000) Role of oxygen vacancy in the plasma-treated $TiO_2$ photocatalyst with visible light activity for NO removal. J Mol Catal A Chem 161:205–212

57. Dong F, Zhao W, Wu Z, Guo S (2009) Band structure and visible light photocatalytic activity of multi-type nitrogen doped $TiO_2$ nanoparticles prepared by thermal decomposition. J Hazard Mater 162:763–770

58. Yang G, Jiang Z, Shi H, Xiao T, Yan Z (2010) Preparation of highly visible-light active N-doped $TiO_2$ photocatalyst. J Mater Chem 20:5301–5309

59. Selvaraj A, Parimiladevi R, Rajesh KB (2013) Synthesis of nitrogen doped titanium dioxide ($TiO_2$) and its photocatalytic performance for the degradation of indigo carmine dye. J Environ Nanotechnol 2:28–31

60. Navio Ja, Cerrillos C, Real C (1996) Photo-induced transformation, upon UV illumination in air, of hyponitrite species $N_2O_2^{2-}$ preadsorbed on $TiO_2$ surface. Surf Interface Anal 24:355–359

61. Saien J, Mesgari Z (2016) Highly efficient visible-light photocatalyst of nitrogen-doped $TiO_2$ nanoparticles sensitized by hematoporphyrin. J Mol Catal A Chem 414:108–115

62. Wang D-H, Jia L, Wu X-L, Lu L-Q, Xu A-W (2012) One-step hydrothermal synthesis of N-doped $TiO_2$/C nanocomposites with high visible light photocatalytic activity. Nanoscale 4:576–584

63. Liu G, Wang X, Wang L, Chen Z, Li F, (Max) Lu GQ, Cheng H-M (2009) Drastically enhanced photocatalytic activity in nitrogen doped mesoporous $TiO_2$ with abundant surface states. J Colloid Interface Sci 334:171–175

64. Lin YT, Weng CH, Hsu HJ, Lin YH, Shiesh CC (2013) The synergistic effect of nitrogen dopant and calcination temperature on the visible-light-induced photoactivity of N-doped $TiO_2$. Int J Photoenergy 2013:1–13

65. Ananpattarachai J, Boonto Y, Kajitvichyanukul P (2015) Visible light photocatalytic antibacterial activity of Ni-doped and N-doped $TiO_2$ on *Staphylococcus aureus* and *Escherichia coli* bacteria. Environ Sci Pollut Res 23:4111–4119